Motion characteristics of large arrays of modularized floating bodies with hinge connections

Deqing Zhang (张德庆),[1,2] Junfeng Du (杜君峰),[1] Zhiming Yuan (元志明),[2] Shuangrui Yu (于双瑞),[2] and Huajun Li (李华军)[1]

[1)]College of Engineering, Ocean University of China, Qingdao, 266100, PR China
[2)]Department of Naval Architecture, Ocean & Marine Engineering, University of Strathclyde, Glasgow, G4 0LZ, UK

(*Electronic mail: dujunfeng@ouc.edu.cn)

(Dated: 31 May 2023)

Hinged arrays have garnered increasing interest due to their potential to provide flexible and adaptable solutions for the various challenges faced in ocean development. The effectiveness of these arrays in engineering applications heavily depends on the motion characteristics of each individual module, rather than specific modules such as the one with the strongest motion. However, the presence of hinge constraints results in coupled motion responses of all modules instead of independent ones. The objective of this study is to investigate the motion behaviour of large arrays formed by multiple floaters hinged together, while existing literature mainly focused on two-body hinged systems. Based on the potential flow theory and Rankine source panel method, a numerical programme was developed to calculate the hydrodynamic interactions and the coupled motion responses. Firstly, a model test was conducted to validate the developed frequency-domain simulations. A good agreement was achieved. Then, the effects of hinge constraints, the number of modules, and two external constraints on the motion responses of the entire array were discussed. The results indicated that the heave motion of the array subjected to hinge constraints was significantly suppressed, but strong pitch motion occurred in a larger wavelength range. For hinged arrays, the floaters located at the two ends were most likely to be excited with the strongest motions. Moreover, a shorter hinged array could be used to quantify the trends in the motion of arrays with more floaters. The calculation results also revealed that the motion responses of a hinged array were highly sensitive to the external constraints, e.g. mooring lines.

I. INTRODUCTION

Large arrays of floating structures are emerging to be an attractive solution for renewable energy production and ocean space utilization. In engineering practice, the operational performance of these arrays is closely related to the motion responses of each module. For example, the pitch motion of a floating photovoltaic (FPV) array significantly affects the angle between the upper solar panels and the sunlight, the electrical conversion efficiency of a raft wave energy converter (WEC) is determined by the relative motions between adjacent floaters, and the behaviour of operational equipment on the multi-use floating islands and the comfort of humans living on them are also closely linked to the motions of the modularized platforms. However, the motion performance of the arrays is significantly affected by the wave motions, hydrodynamic interactions among different modules and the mechanical coupling effect of the connectors.

When water waves impinge on maritime structures, complex interactions occur between the waves and structures. Behera et al. (2018)[1] conducted a study investigating the interaction between oblique waves and a floating plate with three different types of edge conditions. Building upon this research, Selvan and Behera (2020)[2] explored the impact of a porous structure on wave energy dissipation, while Gayathri et al. (2022)[3] examined the effect of porosity of a submerged circular membrane. In a similar vein, Hossain et al. (2023)[4] focused on the influence of the uniform mass and stiffness of a floating plate on the stability of flow beneath it. In another study, Liang et al. (2021)[5] investigated the phenomenon of wave amplification by impermeable plates and found the potential of insights for the applications of floating plates in the ocean engineering, specifically floating breakwaters. Additionally, water wave interaction with box-type structures has also drawn some researcher's attention. Liu and Wang (2020)[6] examined the effects of various cross-sections and physical parameters, such as breakwater density, immersion depth, and ballast-water gravity, on the wave-attenuation performance of box-type breakwaters. Halder et al. (2023)[7] utilized deep learning-driven nonlinear reduced-order models to accurately predict the dynamics of a two-dimensional box floating and interacting with surface water waves. Shi and Zhu (2023)[8] employed a newly proposed spectral coupled boundary element method to investigate the occurrence of gap resonance, a strong nonlinear phenomenon, occurring in the side-by-side offloading of rectangular barges.

For hydrodynamic prediction of large multi-body arrays, a classic study is Kangemoto and Yue (1986)[9], who combined the multiple-scattering interaction theory (Ohkusu, 1974)[10] with the Direct Matrix Method (Simon, 1982)[11] to develop an interaction theory for computing the wave exciting forces and hydrodynamic coefficients of an array consisting of multiple separate cylinders. The accuracy of this theory was validated by the reasonable agreement between their results and the experimental data. Goo and Yoshida (1990)[12] extended Kangemoto and Yue's method (Kangemoto and Yue, 1986)[9] to hydrodynamic interaction for bodies of arbitrary geometry, by utilizing the source distribution panel method and Green's functions in polar coordinates. They compared their numerical results with the experimental results and got a good agreement. Borgarino et al. (2012)[13] implemented a fast multipole

algorithm into the free-surface Green's method to solve the diffracted and radiated wave problems in a generic WEC array. Some limitations of the algorithm were also pointed out, which were attributed to the slow convergence of the expansion of the Green's function. Zhang et al. (2022)[14] proposed a cut-off scheme based on the modularity of bodies in large arrays to address the challenging issue of fully considering the radiation interaction among floating bodies in such configurations. By comparison with the results from the commercial software WADAM[15], it was shown that, while maintaining computational accuracy, the developed cut-off scheme could significantly improve the computational efficiency of hydrodynamic interactions of large arrays.

To ensure the operational safety and maintenance cost of the multi-body system, it is necessary to impose connection constraints between different modules to reduce the risk of collisions or drifting. Just as hydrodynamic interactions between modules can affect their responses, the application of connectors can also have a significant impact on such responses. Diamantoulaki and Angelides (2010)[16] conducted a performance comparison of various configurations of hinged floating breakwaters against a single floating breakwater without hinges. Their results demonstrated that increasing the number of hinge joints could enhance the effectiveness of the floating breakwaters, except for extremely low frequencies and high frequencies. This limitation was attributed to the relatively small dimensions of the array in comparison to the corresponding wavelengths at low frequencies, as well as to low response levels in the short waves. Zheng et al. (2016)[17] examined the influence of three connection conditions on the variation of maximum relative capture width. Their results revealed that the power absorption of the two hinged or rigidly connected rafts can be dramatically reduced. Loukogeorgaki et al. (2017)[18] evaluated the internal forces of connectors in a pontoon-type modular floating breakwater system consisting of flexibly connected and moored chain modules. Each connector in their study was made of coated wire rope, and its flexibility was expressed by the axial and bending stiffness. Zhao et al. (2019)[19] proposed a general approach to determine the stiffness configuration for various wave conditions by simplifying the connector and ignoring its torsional and bending stiffness. It indicates that the combination of small longitudinal stiffness, large transversal and large vertical stiffness is favourable for motion under most wave conditions. Xia et al. (2020)[20] applied a control method in conjunction with hinged connectors to suppress the heave, roll and pitch motions of a five-modular floating structure. Their numerical simulations verified the effectiveness of the combination of the control strategy and hinge connection. Ma et al. (2022)[21] examined the dynamic behaviors of a hinged two-body floating aquaculture platform under regular waves. Their results showed that the hinge-joint rotational stiffness has a predominant influence on the maximum pitch response.

Among the various types of connection constraints, hinge joints are a commonly used form of connector in large arrays, which serve to restrict the relative motion between adjacent modules. They are typically assembled in the gap space between two adjacent to restrict their relative motion around the
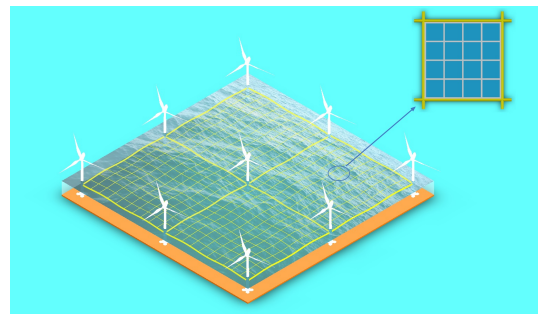
(a)
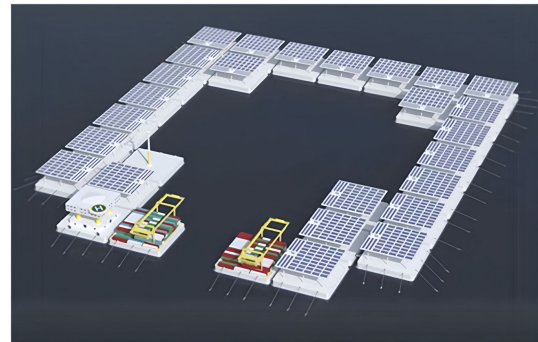
(b)

FIG. 1. Sketch of two applications of large arrays of modularized floating bodies with hinge connections. (a) A FPV array (Zhang et al., 2023); (b) a multi-use floating island of Energyhub@Sea (Flikkema et al., 2021).

axis of the hinge connector, reducing the risk of collisions or drifting. Some studies have been published to demonstrate how to accurately predict the motion response of each floater in a hinged multi-body system. Newman (1994)[22] firstly took hinge constraints into consideration in multi-body problems. He utilized a mode generalized method to predict the vertical motion and relative rotation of a hinge in a two-barge system. Sun et al. (2011)[23] applied the Lagrange multiplier technique to investigate the same interconnected barge configuration. They compared their numerical results with Newman's results (Newman, 1994)[22] and got a good agreement. Zheng et al. (2015)[24] used a method of introducing a constraint matrix into the frequency domain dynamics equations to calculate the results of motion. Their results also agree well with Newman's results (Newman, 1994)[22]. Compared to the study of motion response predictions of hinged multi-body systems, an increasing number of researchers are now more focusing on the practical application of hinged arrays. Ren et al. (2019)[25] investigated the effects of various combinations of hinges, linear pitch springs, and linear pitch dampers on the shear force, bending moment of connectors, and the motion of modules. Their findings indicated that using a hinge-PTO-type design for the outermost connector can effectively reduce the motion of the outermost module. Jiang et al. (2021)[26] employed a potential-flow-based numerical model to investigate the hydrodynamic sensitivity of an articulated modular floating structure. Their results showed that the hydrodynamic
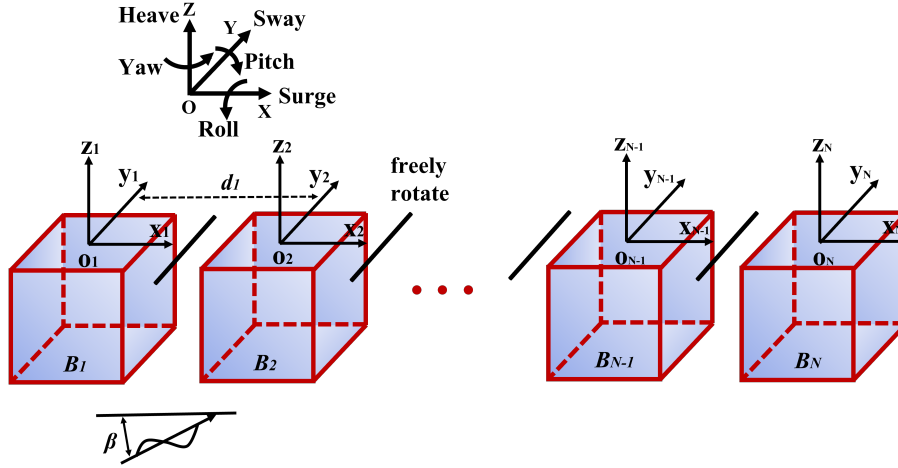
FIG. 2. Coordinate systems.

properties were similar for arrays of different number of modules, but that the translational horizontal motions were very sensitive to the incident wave angle. Liu et al. (2022)[27] conducted numerical simulations to analyze the hydrodynamic responses of a novel hybrid modular floating structure system. The results demonstrated that this hybrid system showed good longitudinal expansibility for mild marine environments. Bispo et al. (2022)[28] developed a numerical model to examine the interaction of waves with a set of hinged plates. The study found that the rotational stiffness of the hinges greatly affects the vertical displacement of the structure. Previous studies typically focused on selecting several variables as target parameters, such as the maximum motion of modules or the maximum internal force of connectors. However, investigating the motion response characteristics of all modules in the entire array is crucial for arranging the upper facility and monitoring the overall health of the array. This will be the objective of the present study.

In the present study, a 3-D panel code based on the Rankine source method, named MHydro, is developed to investigate the motion characteristics of large arrays with hinge constraints. The fully hydrodynamic interactions among modules and the mechanical coupling effect of the hinges are considered in the analysis. The remainder of this paper is structured as follows. Section 2 provides a description of the application and simplification of hinged arrays. Section 3 outlines the numerical methodology for analyzing the hydrodynamic interactions and motion responses of hinged arrays. A hinged multi-body model test is conducted to validate the in-house numerical code, and the results can be found in Section 4. The validated numerical code is then applied to carry out a multi-parameter study in Section 5. Finally, Section 6 summarizes the conclusions.

II. PROBLEM DESCRIPTION

Large arrays typically consist of dozens or even hundreds of modularized floating bodies that are interconnected by hinge constraints. These floating modules usually have identical geometric parameters to facilitate manufacturing, assembly, and maintenance. The motion responses of all modules are coupled due to the presence of hinge constraints, which in turn reduces the likelihood of collisions or separations between them. The concept of hinged arrays has been widely applied to many offshore engineering practices. Fig. 1 illustrates two common engineering applications: a FPV array for converting solar energy into electrical energy (Zhang et al., 2023)[29], and a multi-use artificial island used to supply energy for other marine equipment (Flikkema et al., 2021)[30].

The aim of the present study is to conduct fundamental research on the motion characteristics of hinged arrays, and thus the floating modules are not designed at full-scale dimensions in this paper. In actual engineering applications, the size of the modules can be determined based on specific marine conditions and the conclusions drawn from this study. Furthermore, considering the variability in the layout of hinged arrays, the arrays are simplified to only be arranged along the longitudinal direction (chain type) in this study. The hinge axes are assembled along the y-axis at the midline of the gap between two adjacent floating bodies, allowing only the pitch motion to be free. The influence of other complex arrangements on the motion responses of hinged arrays will be further investigated in future studies.

III. NUMERICAL METHODOLOGY

In order to conduct the present investigation, we employed a boundary element programme MHydro, which is based on potential flow theory and Rankine source panel method, to calculate the motion performance of hinged arrays. Yuan et al. (2014, 2015)[31][32] gave the details about using MHydro to solve the ship-to-ship problem. The same method and numerical programme will be used in the present study.

A. Coordinate systems

Considering N bodies oscillating in open sea, the corresponding right-handed coordinate systems are shown in Fig. 2. $O - XYZ$ is the global coordinate system with its origin fixed on the undisturbed free surface and $O - Z$ axis is positive upwards. The body coordinate systems $o_m - x_m y_m z_m (m = 1, 2, \ldots, N)$ are fixed on each body with their origins locating on the mean free surface at midships and $o_m - z_m$ pointing upwards. d_m and l_m represent the transverse and longitudinal distance between the m-th body coordinate system and the global coordinate system, respectively. In the present study, the global coordinate system $O - XYZ$ coincides with the first body-fixed coordinate system $o_1 - x_1 y_1 z_1$. The incident wave direction β is assumed as the angle between the wave propagation direction and the positive X-axis, with $\beta = 0°$ corresponding to the head wave.

The positive 6 degrees of freedom (DoF) are also shown in Fig. 2. In the computation, the motions and forces of each body are transferred to the body-fixed coordinate system.

B. Diffraction wave potential

With bodies in the wave field, the propagation of the incident waves will be affected, and the diffracted waves will be generated. Assuming the surrounding fluid is ideal, the velocity potential which satisfies the Laplace equation in the whole fluid is introduced. The linearized diffraction potential can be expressed as

$$\Psi_D(\vec{X}, t) = Re[\eta_7 \varphi_7(\vec{X}) e^{-i\omega_0 t}] \tag{1}$$

where $Re(*)$ denotes the real part of the argument; φ_7 is the unit diffraction potential and $\eta_7 = \eta_0$ is the incident wave amplitude; ω_0 is the incident wave frequency.

The linearized incident wave velocity potential φ_0 is described as

$$\varphi_0 = -\frac{ig\eta_0}{\omega_0} \frac{\cosh k(z+d)}{\cosh kd} e^{i[k(x\cos\beta + y\sin\beta)]} \tag{2}$$

where d is the water depth; β is the angle of wave heading; and k is the wave number that satisfies the dispersion relation

$$k \cdot \tanh kd = \omega_0^2 / g \tag{3}$$

The Laplace equation and linearized boundary conditions used to solve the diffraction velocity potential are summarized as follows:

$$\nabla^2 \varphi_7 = 0 \qquad \text{in the fluid domain;} \tag{4}$$

$$g\frac{\partial \varphi_7}{\partial z} - \omega_0^2 \varphi_7 = 0 \quad \text{on the undisturbed free surface } S_f; \tag{5}$$

$$\frac{\partial \varphi_7}{\partial n} = -\frac{\partial \varphi_0}{\partial n}\Big|_{S_m} \quad \text{on the mean wetted surface } S_m; \tag{6}$$

$$\frac{\partial \varphi_7}{\partial z} = 0 \qquad \text{on the seabed.} \tag{7}$$

C. Radiation wave potential

The radiated waves are generated by the oscillation of the bodies. For linearization, the radiation velocity potential can be written as follows:

$$\Psi_R(\vec{X}, t) = Re \sum_{j=1}^{6} \sum_{m=1}^{N} \left[\eta_j^m \varphi_j^m (\vec{X}) e^{-i\omega_0 t} \right] \tag{8}$$

where $\varphi_j^m (j = 1, 2, \ldots, 6; m = 1, 2, \ldots, N)$ is the unit radiated wave potential in the j-th DoF corresponding to the m-th body; $\eta_j^m (j = 1, 2, \ldots, 6; m = 1, 2, \ldots, N)$ is the corresponding oscillation amplitude (η_1: surge; η_2: sway; η_3: heave; η_4: roll; η_5: pitch; η_6: yaw). The radiation velocity potential can be solved by the following boundary value problem:

$$\nabla^2 \varphi_j^m = 0, \quad j = 1, 2, \ldots, 6 \qquad \text{in the fluid domain;} \tag{9}$$

$$g\frac{\partial \varphi_j^m}{\partial z} - \omega_0^2 \varphi_j^m = 0,$$
$$j = 1, 2, \ldots, 6 \qquad \text{on the undisturbed free surface } S_f; \tag{10}$$

$$\frac{\partial \varphi_j^m}{\partial n} = \begin{cases} -i\omega_0 n_j|_{S_m}, \\ 0|_{S_{others}} \end{cases},$$
$$j = 1, 2, \ldots, 6 \qquad \text{on the mean wetted surface } S_m; \tag{11}$$

$$\frac{\partial \varphi_j^m}{\partial z} = 0 \qquad \text{on the seabed.} \tag{12}$$

Moreover, a suitable Sommerfeld radiation condition must be imposed on the control surface to complete the above boundary value problem. The generalized normal vectors are expressed as

$$n_j = \begin{cases} \vec{n}, & j = 1, 2, 3 \\ \vec{x} \times \vec{n}, & j = 4, 5, 6 \end{cases} \tag{13}$$

where $\vec{n} = (n_1, n_2, n_3)$ is the unit normal vector directed inward on body surface S_m; $\vec{x} = (x, y, z)$ is the position vector on S_m.

The entire computational domain consists of the body-, free-, control- surface and seabed. In the numerical study, the boundary is discretized into multiple quadrilateral panels with varying source density. The velocity potential on each boundary panel is solved using the Rankine-type Green function. Detailed information regarding the numerical implementation can be found in the work by Zhang et al. (2022)[14].

D. Equations of hinged multi-body motion

Once the unknown diffraction velocity potential φ_7 and radiation velocity potential φ_j^m are obtained, the pressure on each body surface can be derived from Bernoulli's equation,

$$p_j^m = -i\omega\rho \varphi_j^m, \quad j = 0, 1, \ldots, 6, 7; m = 1, 2, \ldots, N \tag{14}$$

where ρ is the fluid density.

The wave excitation force can then be obtained by the integration of incident and diffraction pressure on the wetted body

$$F_i^{R_m} = \sum_{j=1}^{6} \iint_{S_m} p_j^m n_i dS \cdot \left(\sum_{n=1}^{N} \eta_j^n \right) = \sum_{j=1}^{6} \sum_{n=1}^{N} \left(\omega_0^2 \mu_{ij}^{mn} + i\omega_0 \lambda_{ij}^{mn} \right) \eta_j^n, \ i,j = 1, 2, \ldots, 6; \ m,n = 1, 2, \ldots, N \quad (16)$$

where μ_{ij}^{mn} is the added mass coefficient of B_m in the i_{th} mode which is induced by the oscillation motion of B_n in the j_{th} mode; λ_{ij}^{mn} is the damping coefficient in which the definitions of subscript and superscript are the same as those of added mass. The added mass and damping coefficients can be written as

$$\mu_{ij}^{mn} = -\frac{\rho}{\omega_0} \iint_{S_m} \varphi_{Ij}^n n_i dS, \ i, j = 1, 2, \ldots, 6; \ m, n = 1, 2, \ldots, N \quad (17)$$

$$\lambda_{ij}^{mn} = \rho \iint_{S_m} \varphi_{Rj}^n n_i dS, \ i, j = 1, 2, \ldots, 6; \ m, n = 1, 2, \ldots, N \quad (18)$$

where φ_{Ij} donates the imaginary part of j_{th} radiation potential, and φ_{Rj} is the real part.

Based on Newton's second law, the motion equation of free-floating bodies in frequency domain can be expressed as

$$\left[-\omega^2 \mathbf{M} - i\omega \mathbf{B} + \mathbf{K} \right] \{\eta\} = \{\mathbf{F}\} \quad (19)$$

where $\mathbf{M}$, $\mathbf{B}$ and $\mathbf{K}$ are the mass, damping and stiffness matrix, respectively; η is the displacement matrix; $\mathbf{F}$ is the external forces matrix, which includes the wave excitation force F^W and the hydrodynamic forces F^R. It should be noted that the structure damping is assumed to be zero in this study. By rearranging the equation and shifting the hydrodynamic forces to the left of the motion equation, the equation can be expressed as

$$\left[-\omega^2 (\mathbf{M} + \mu) - i\omega\lambda + \mathbf{K} \right] \{\eta\} = \left\{ \mathbf{F}^W \right\} \quad (20)$$

Thus, the motion of B_m in the i-th mode can be described in detail as

surface as

$$F_i^{W_m} = \iint_{S_m} (p_0 + p_7) n_i dS \quad (15)$$

Moreover, the hydrodynamic forces induced by the oscillatory motions of B_m in the i_{th} direction can be expressed as

$$\sum_{j=1}^{6} \left\{ [-\omega_0^2 (M_{ij}^m + \mu_{ij}^{mm}) - i\omega_0 \lambda_{ij}^{mm} + K_{ij}^m] \eta_j^m + \sum_{n=1,n \neq m}^{N} (-\omega_0^2 \mu_{ij}^{mn} - i\omega_0 \lambda_{ij}^{mn}) \eta_j^n \right\} = F_i^{W_m}, \quad (21)$$
$$i, j = 1, 2, \ldots, 6; \ m, n = 1, 2, \ldots, N$$

where the term related to η_j^n is the hydrodynamic forces on B_m generated by the radiation motions in 6 DoF performed by the structures excluding B_m.

If a hinge constraint along the y-axis is applied between two bodies, the displacements in five DoFs (surge, sway, heave, roll, and yaw) are continuous at the hinge joint and the pitch motion is free. There are thus five constraints between two interconnected m-th and $(m+1)$-th bodies and the corresponding constraint equations are

$$\eta_1^m + \eta_5^m z^m - \eta_6^m y^m = \eta_1^{m+1} + \eta_5^{m+1} z^{m+1} - \eta_6^{m+1} y^{m+1}$$
$$\eta_2^m - \eta_4^m z^m + \eta_6^m x^m = \eta_2^{m+1} - \eta_4^{m+1} z^{m+1} + \eta_6^{m+1} x^{m+1}$$
$$\eta_3^m + \eta_4^m y^m - \eta_5^m x^m = \eta_3^{m+1} + \eta_4^{m+1} y^{m+1} - \eta_5^{m+1} x^{m+1} \quad (22)$$
$$\eta_4^m = \eta_4^{m+1}$$
$$\eta_6^m = \eta_6^{m+1}$$

where (x^m, y^m, z^m) and $(x^{m+1}, y^{m+1}, z^{m+1})$ are the coordinates

of a hinge joint in the m-th and $(m+1)$-th body-fixed coordinate systems, respectively. Similarly, if the hinge constraint is applied along the x-axis, then only the roll motion is free. The dynamic equation of motion for the hinged multi-body array in the frequency domain can be written as

$$\begin{bmatrix} -\omega_0^2 (\mathbf{M} + \mu) + i\omega_0 \lambda + \mathbf{K} & \mathbf{D}_J^T \\ \mathbf{D}_J & \mathbf{0} \end{bmatrix} \begin{Bmatrix} \eta \\ \mathbf{F}_J \end{Bmatrix} = \begin{Bmatrix} \mathbf{F}^W \\ \mathbf{0} \end{Bmatrix} \quad (23)$$

where $\mathbf{M}$ and $\mathbf{K}$ are the array mass and stiffness matrix of $(6N \times 6N)$, respectively; μ and λ are the array added mass and potential damping matrix of $(6N \times 6N)$; $\mathbf{D}_J$ is the displacement constraint matrix of $(Q \times 6N)$, in which Q represents the number of hinge joint constraints; η is the frequency-dependent displacements matrix of $(6N \times 1)$; $\mathbf{F}_J$ is the joint force vector of $(Q \times 1)$; $\mathbf{F}^W$ is the wave excitation force array of $(6N \times 1)$.
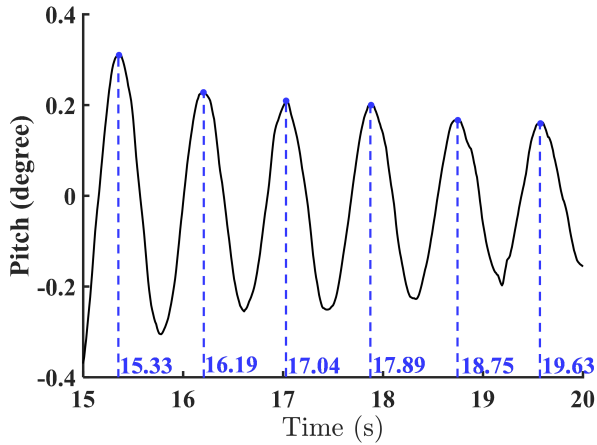
FIG. 3. Free decay motion of the box in pitch direction.

TABLE I. Main parameters of identical box model.

Parameters	Values
Length	L_b=0.4 m
Width	B_b=0.25 m
Height	D_b=0.2 m
Draft	h_b=0.1 m
Mass	m_b=9.633 kg
Centre of gravity	z_G=-0.027 m

IV. VALIDATIONS

A validation of the developed numerical programme MHydro is now considered via the comparison with model test results. Two cases with different model numbers are tested individually, a single box system and a hinged 5-box system. All models have identical geometry dimensions and physical properties. The main particulars of the identical box model are shown in Table I. The second moment of the water plane about the y-axis can be obtained by the equation $I_{w2} = B_b L_b^3/12$=0.0013 m^4. The model test is conducted in a flume tank with a main dimension of 6.7 m length, 3.15 m width and 1.35 m height at the Kelvin Hydrodynamic Laboratory of University of Strathclyde. The incident wave direction is $\beta = 180°$, the water depth is d=1 m and the incident wave amplitude is A=0.01 m. A Qualisys system was applied to track the motion time series of the physical models (Yiew et al., 2017)[33]. Fig. 3 illustrates the free decay pitch motion of a single model. The box model has a very large restoring stiffness in the pitch direction, and a small external load is applied during the free decay test. This explains why the free decay results in Fig. 3 are small. Furthermore, it should be noted that the external force is not released until 15 s, which explains the absence of pitch motion in Fig. 3 prior to that time. Based on the results of the free decay test, the natural frequency of a box model ω_n=7.306 rad/s is obtained to compute the pitch moment of inertia $M_{55} = 0.128$ kg$\cdot$m^2. Once the physical properties of each model are derived, the 5-box models are interconnected along the longitudinal direc-
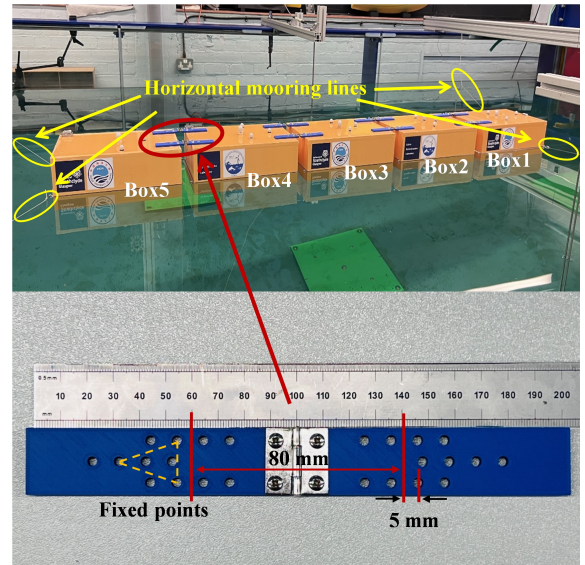

FIG. 4. Photos of the hinged 5-box system and the hinge assembly. The gap distance between adjacent boxes is 0.08 m. Two hinges are assembled on the midline of each gap.
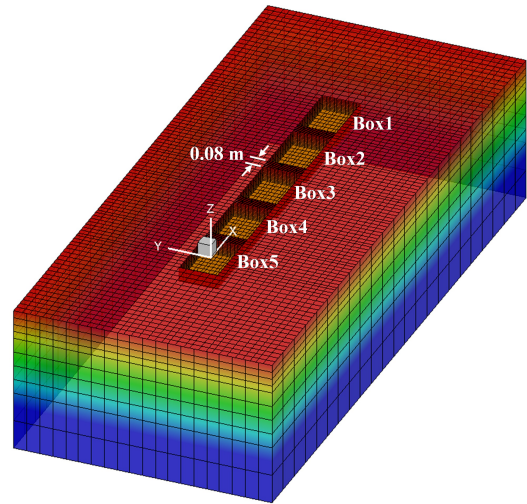

FIG. 5. Computational domain of the 5-box model in head wave. The free surface is truncated at $1.5L_b$ upstream, $1.5L_b$ downstream, and $3B_b$ sideward. There are 500 panels on each box surface, 3,220 panels on free surface, and 860 panels on control surface.

tion with hinges assembled at the midline of the 0.08 m gap. The hinged 5-box system and the hinge assembly are shown in Fig. 4. A horizontal mooring system is employed to ensure that the model system can be restored to its original position after the wave maker stops running, by providing additional restoring forces in the surge, sway, and yaw directions. This mooring system comprises of four horizontal light mooring lines, with each line connected to one of the four corners of the model system. As shown by the yellow dashed lines, three holes on the hinge are used to keep the hinge from moving relative to the connected box. The distance between adjacent
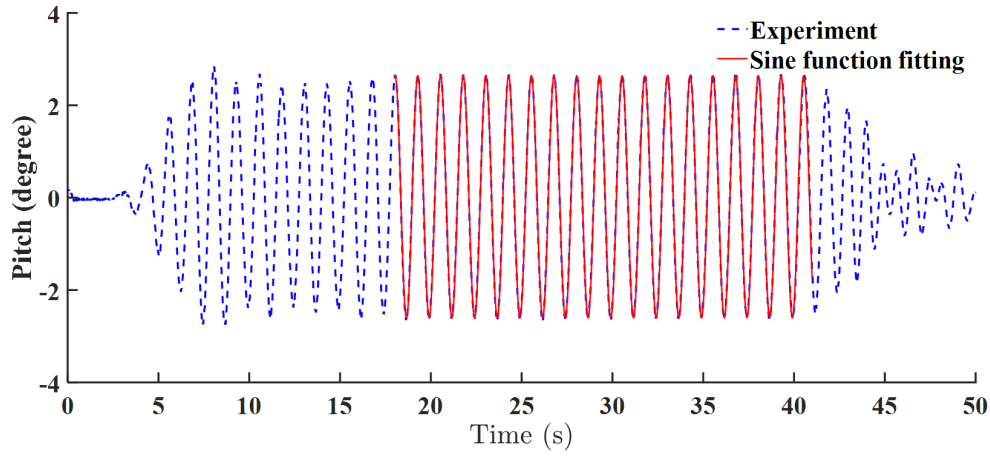
FIG. 6. Time series of pitch motion of Box1 at a wavemaker input frequency of 5.0265 rad/s. The blue dashed line represents the actual results tracked in the tank, and the red solid line shows the results of the curve fitting using a sine function.
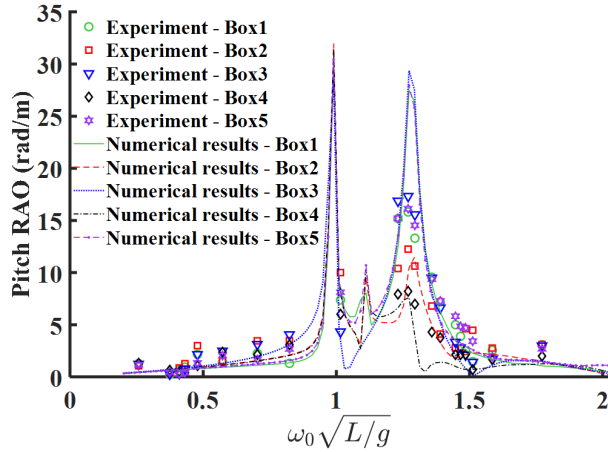

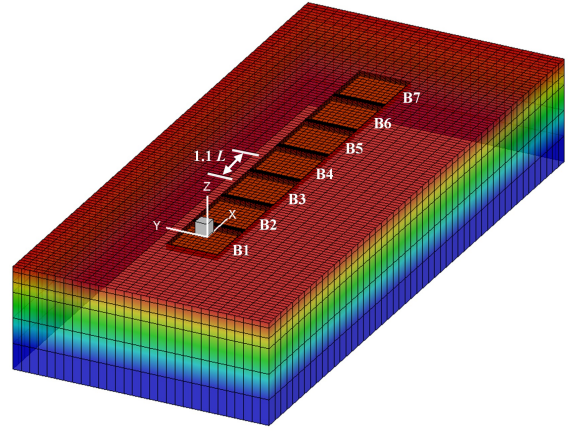FIG. 7. Response amplitude operators of pitch motions of the hinged 5-box array.

FIG. 8. Computational domain and panel distribution of the numerical model for a hinged 7-box array at wavelength $\lambda/L=1$. A box of dimensions at $B/L=1$, $D/L=0.1$, respectively. The gap distance d between two adjacent boxes is $0.1L$. The size of the free surface is wavelength dependent: truncated at 2λ upstream, 2λ downstream, and $2L$ sideward. There are 8,060 panels distributed on the entire computational domain: 300 on each body surface, 4,680 on the free surface and 1,280 on the control surface.

boxes can be changed by adjusting the position of three fixed points. However, the effect of gap distance is not discussed in this study. The numerical simulation adopts the same geometric situation as that used in the model test. The panels of the computational domain are shown in Fig. 5.

To obtain the motion RAOs of the models, tests are required with the models exposed to regular waves. To ensure accurate results, data should be collected for no less than 10 full wave cycles during the regular wave tests, as recommended by the International Towing Tank Conference (ITTC, 2002)[34]. Taking the case of a wavemaker input frequency of 5.0265 rad/s as an example, we will describe the procedure for obtaining the Pitch RAO. Fig. 6 shows the time series of pitch motion of Box1. As shown in Fig. 6, the steady range of the acquired motion response is fitted with a Sine function to obtain the amplitude, frequency, and phase information. By fitting the pitch motion in Fig. 6 with a Sine function, the amplitude of the motion is determined to be $2.6224°$, with a frequency of 5.0265 rad/s. Due to the limitations of the wavemaker and the

tank, it may not be possible to precisely replicate the same wave as that fed into the wavemaker. Hence, the free surface elevation also needs to be recorded and fitted using the Sine function. The fitting analysis of the wave elevation reveals an amplitude of 0.0062 m and a frequency of 5.0265 rad/s. To facilitate comparison, the unit of pitch motion is converted to radians. As a result, the pitch motion RAO at the non-dimensionalized frequency of 1.0155 is 7.3822 rad/m. Similarly, the RAO of pitch motion at other frequencies is obtained using the same approach. The comparison of pitch motion between the present numerical results and experimental data is shown in Fig. 7. In the model test, a total of 20 wave frequencies were individually input into the wavemaker, and the corresponding motion RAO results were obtained. Each fre-
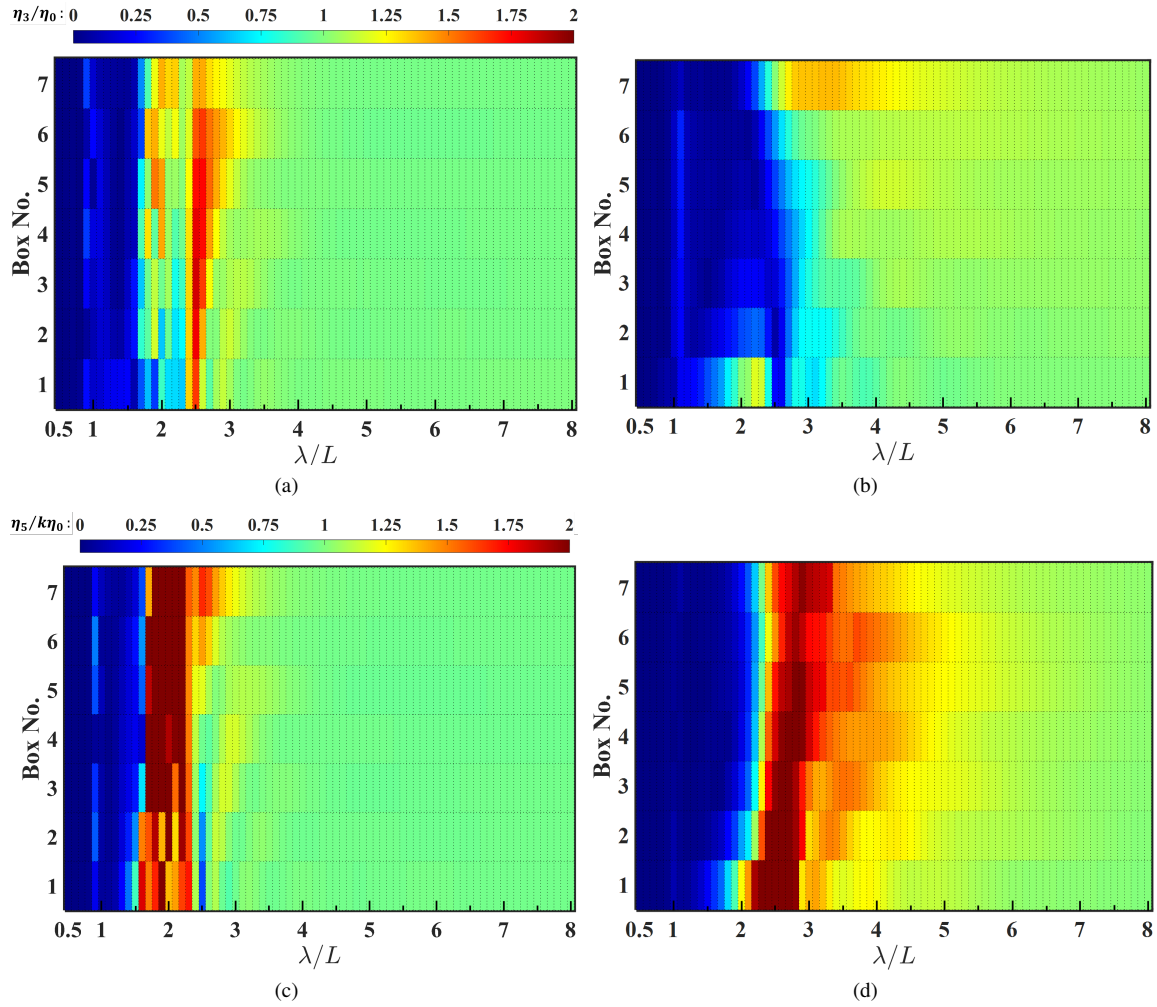
FIG. 9. Heave and pitch motion of free-floating and hinged 7-boxs arrays. The heave motion is non-dimensionalized by the wave amplitude η_0 and the pitch motion is non-dimensionalized by the wave steepness $k\eta_0$. (a) Heave motion of free-floating boxes array; (b) heave motion of hinged boxes array; (c) pitch motion of free-floating boxes array; and (d) pitch motion of hinged boxes array.

quency and its corresponding pitch RAO can be found in Fig. 7. For the numerical simulations, the spacing of wave frequencies was refined to achieve smoother result curves. Larger peak results can be observed in the numerical results. This is due to the fact that the viscous effect is ignored in the present numerical programme. The numerical results calculated by the present programme generally agree well with the experimental data, indicating that the body motion responses of hinged multi-body arrays can be predicted by the present 3-D Rankine source programme.

V. RESULTS AND DISCUSSIONS

The validated numerical programme is applied to a series of case studies to investigate the influence of various parameters, e.g. hinge connection, number of modules, external stiffness constraint, and array arrangement configuration, on the motion characteristics of large hinged arrays.

A. Comparisons of free-floating and hinged boxes arrays

Large arrays of modularized floating structures are typically connected by hinge joints, which strongly affect the motion performance of the arrays. Two case studies are designed here, based on 7 identical floating boxes oscillating side by side in head waves, to investigate the effect of hinge connections. The main particulars of the identical boxes are $B/L=1$ and $D/L=0.1$, respectively. The longitudinal and transverse distance between two adjacent boxes is $1.1L$ and 0, respectively. In the present study, a reference length of $L=1$ m is chosen as the main dimension. Other essential reference parameters include a mass of 102.5 kg, a roll moment of inertia of 8.627 kg·m^2, a pitch moment of inertia of 8.627 kg·m^2, a yaw moment of inertia of 17.08 kg·m^2, and a centre of gravity located on the calm free surface. However, it is worth noting that in this study, both the physical particulars and computational results have been non-dimensionalized. This approach allows us to quantify the underlying principles that are inde-
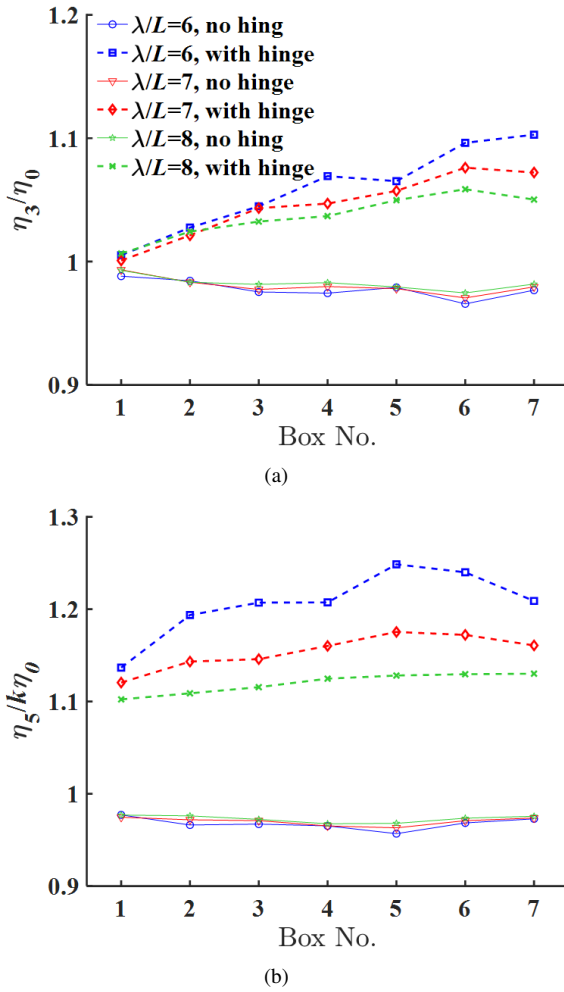
FIG. 10. Heave and pitch motion of free-floating and hinged 7-boxes arrays at wavelengths λ/L=6, 7, and 8.

pendent of specific scales or units, and facilitates the application of the findings to different scales or sizes in real-world scenarios. The computational domain and discretization of the boundaries is presented in Fig. 8. For the present hinged array, the hinge joints are assembled on the undisturbed waterline plane, i.e. z^m=0. In this study, the authors would like to concentrate on wave incident angle $\beta = 0°$, thus the number of DoFs for the motion of each body can be reduced to only surge, heave, and pitch. Additionally, the surge motion is identical for each module. Therefore, only the heave and pitch motion of each module are of particular interest in this paper.

Fig. 9 shows the heave and pitch motion of each module at different wavelengths. The non-dimensionalization for heave motion is made by the incident wave amplitude η_0, while the non-dimensionalization for pitch motion is made by the wave steepness $k\eta_0$. It can be clearly found that the motion colormap of the free-floating boxes array is much messier compared to the motion results of the hinged array. It indicates that when the hinge joints are assembled between the floaters, the wavelengths at which the floaters would be strongly excited become more concentrated. For example, the pitch motion of the hinged B1 in Fig. 9 (d) shows a very significant peak around λ/L=2.3, while the response of B1 with independent oscillations is clearly chaotic around the wavelengths λ/L=1.7-2.2 where the pitch motion is strong. From Fig. 9 (b) and (d), we can see that when the floaters are hinged, the colormap of heave motion is basically devoid of red and orange regions, except for B7 around λ/L=3.3. However, there is a significant increase in the red and orange areas of the pitch colormap. This means that there will essentially be no longer strong heave motions when the hinges are assembled in the array, but noticeable pitch motions will occur over a wider wavelength range. As outlined in Section 2, the application of a hinge joint along the y-axis between two adjacent bodies allows only the pitch motion is unrestricted, while the other five DoFs are constrained. Specifically, these constrained motions must maintain continuity at the hinge point. Additionally, the module experiences forces in the z-direction induced by the waves, but its displacement in the z-direction is limited due to the presence of hinge joints. However, this constraint at the hinge point results in the release of some of the vertical forces into moments around the hinge point. This explains why the heave motion of the hinged array is suppressed while the pitch motion is easy to be excited. Meanwhile, by comparing the four figures in Fig. 9, it can also be seen that when the floaters are hinged, the blue regions of both the heave and pitch motion colormap become significantly greater at short wavelengths. It suggests that longer wavelengths are required for the floaters to be significantly excited when they are hinged. However, at long wavelengths, the colormaps of the free-floating floaters have more distinct green regions, which represent smaller motion responses. Fig. 10 shows the heave and pitch motion of two arrays at long wavelengths λ/L=6, 7, and 8. As with the results shown in the motion colormap, both the heave and pitch motion of the hinged floaters are noticeably greater than the motion of floaters with independent oscillations at long wavelengths. It can also be observed from Fig. 10 that the response of the floaters at the trailing end of the hinged array is significantly greater than that of the floaters at the front end. Besides, as the wavelength increases, the non-dimensionalized motions of the floaters in both arrays are convergent to 1. This is due to the fact that when the waves are long enough, the near-zero values of the inertia and damping terms in the motion equation enable the floaters will travel with the waves.

Fig. 11 shows the statistical results of the motion colormaps presented in Fig. 9. The bars in the charts indicate the proportion of a particular floater that shows the strongest responses in the array across the entire wavelength range. And the lines represent the average response value of the responses of a given floater when it displays the strongest response. For the strongest heave motion of the free-floating array, the sixth floater shows the highest proportion, up to 0.6, while its adjacent floater B5 has the strongest response at only a very few wavelengths. Moreover, except for B5, the mean values of the maximum heave motion of the other floaters are large. This indicates that the maximum heave motions of most floaters are relatively large when there is no hinge constraint. This can be
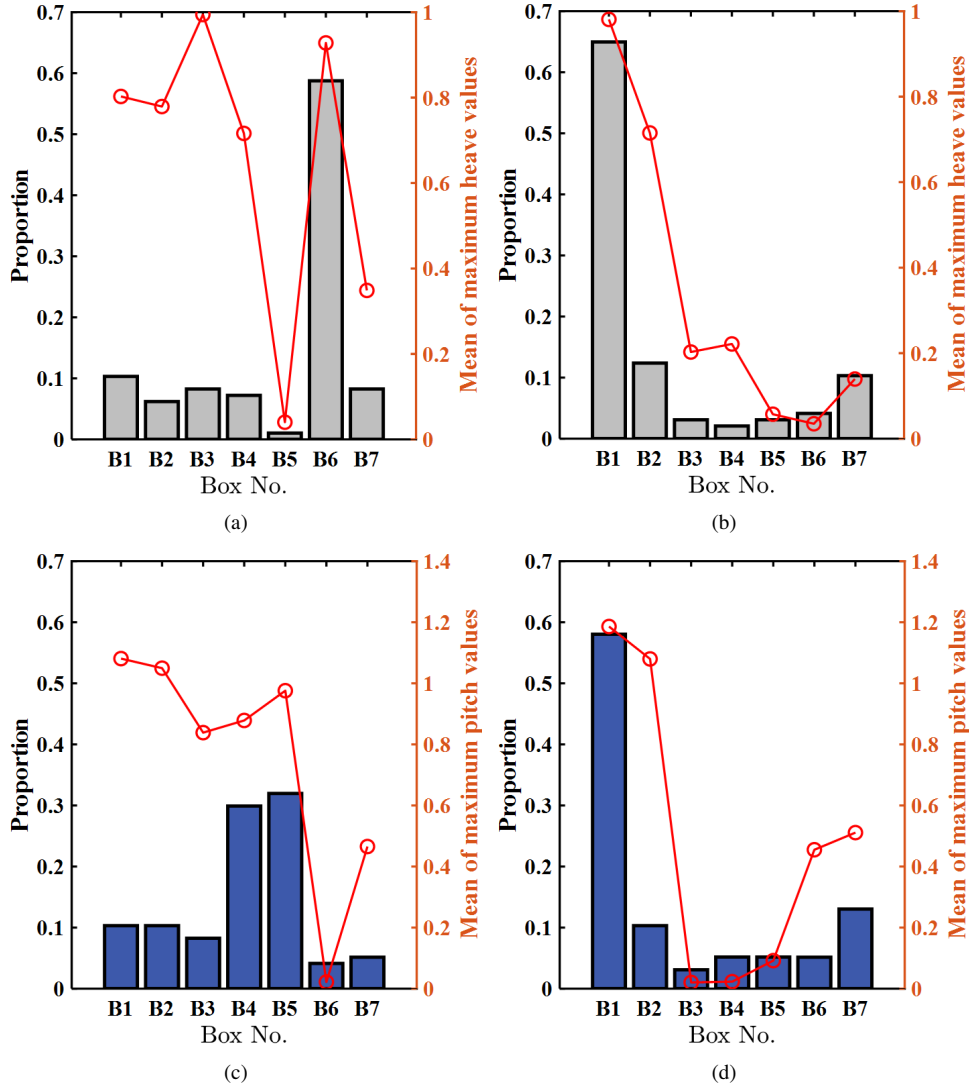
FIG. 11. Proportion of floating bodies with the strongest responses and mean values of the maximum motions. The statistical range of wavelengths is from $0.5L$ to $8L$ at $0.1L$ intervals. The right y-axis is the average of the non-dimensionalized maximum values. (a) Statistical results of heave motion of an array of free-floating 7-bodies; (b) statistical results of heave motion of an array of hinged 7-bodies; (c) statistical results of pitch motion of an array of free-floating 7-bodies; and (d) statistical results of pitch motion of an array of hinged 7-bodies.

explained by Fig. 9 (a), where less blue area indicates that larger oscillations are more likely to occur. Different from the results shown in Fig. 11 (a), in the hinged case, the first floater accounts for the highest ratio of over 0.65 as shown in Fig. 11 (b). The proportions of floaters located in the middle of array are relatively lower, and the mean values are also smaller, indicating that they are less likely to be excited to generate a large heave motion. Similar to the heave motion of hinged floaters, the middle-positioned floaters have a low proportion of the maximum pitch motion. The floater with the highest ratio is also the first floater, followed by the last floater. However, when the floaters are free-floating, the proportions of these two floaters become significantly lower, and the floaters located in the middle position have a higher proportion. From Fig. 11 (d), large average values of the maximum pitch motion only can be found in several floaters located at the ends

of the hinged array. As a result, for the arrays of hinged floating bodies, the motion responses of several floaters at either end, especially the first couple of floaters in the weather side, should be of particular interest.

B. Longitudinal expansibility of hinged boxes arrays

The arrays of hinged floating structures can provide a larger deck area by increasing the number of modules, allowing more marine equipment to work simultaneously or providing a greater living space for people. Fig. 12 shows a sketch of an array of $N \times 1$ hinged floating bodies. To investigate the longitudinal expansibility of hinged bodies arrays, four arrays with different numbers of modules are designed, with N being 5, 7, 10, and 14 respectively. Fig. 13 and Fig. 14 show the
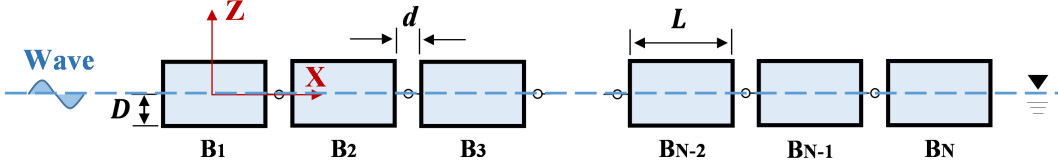
FIG. 12. Sketch of $N \times 1$ hinged boxes array.

(a)

(b)

(c)

(d)
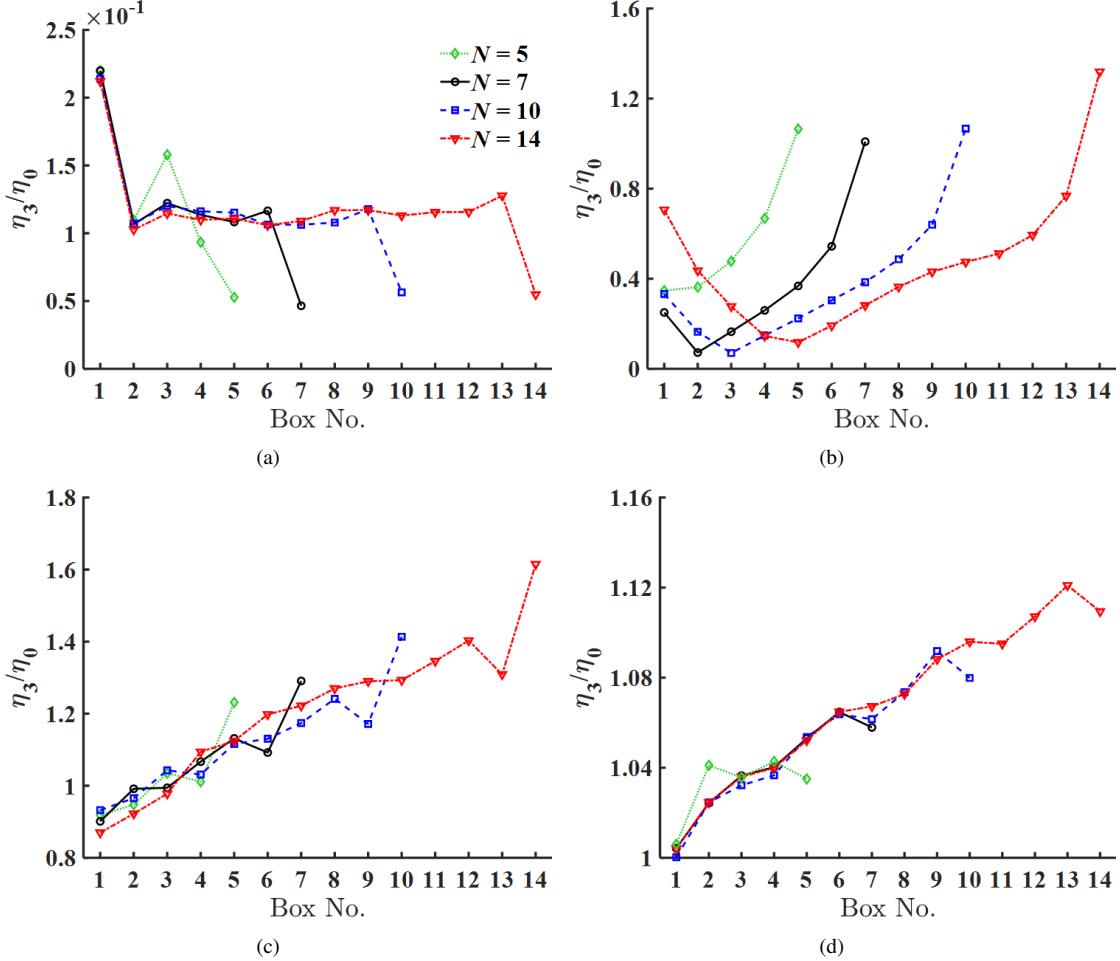
FIG. 13. Heave motion of four arrays with different number of hinged boxes at four typical wavelengths. (a) λ/L=1.1; (b) λ/L=2.4; (c) λ/L=3.8; (d) λ/L=7.6.

heave and pitch motions of these four arrays at four typical wavelengths of λ/L=1.1, 2.4, 3.8, and 7.6, respectively. The four wavelengths are chosen based on the motion colormap shown in Fig. 9: a short wave with very weak motions for the hinged 7-boxes array, two intermediate waves with strong motion responses, and a long wave where the array basically travels with the wave. From Fig. 13 and Fig. 14, we can find the motion responses of all four arrays have essentially the same trend at the same wavelength. Similar observations were made by Jiang et al. (2021)[26] in the case of hydrodynamic sensitivity of a hinged modular floating structure to the number of modules. However, special attention should be paid on the motion responses of the 5-box array. Although the 5-box

array shows a similar overall trend to the other three arrays, the trend of the 5-box array differs in detail at some wavelengths. Taking Fig. 13 (a) as an example, the heave responses of the first floater is significantly larger and the response of the last one is noticeably smaller, while the trend of the responses of the other floaters are very smooth. However, the responses of the middle-positioned floaters in the 5-box array are clearly jerkier. It is very interesting to find that when the array is subjected to short or long waves, the motion responses of the front-end floaters in the three long arrays are largely overlap. Combining the conclusion from sub-section 5.1 that the hinged array exhibits an overall increase in heave and pitch motions at long wavelengths, it can be concluded
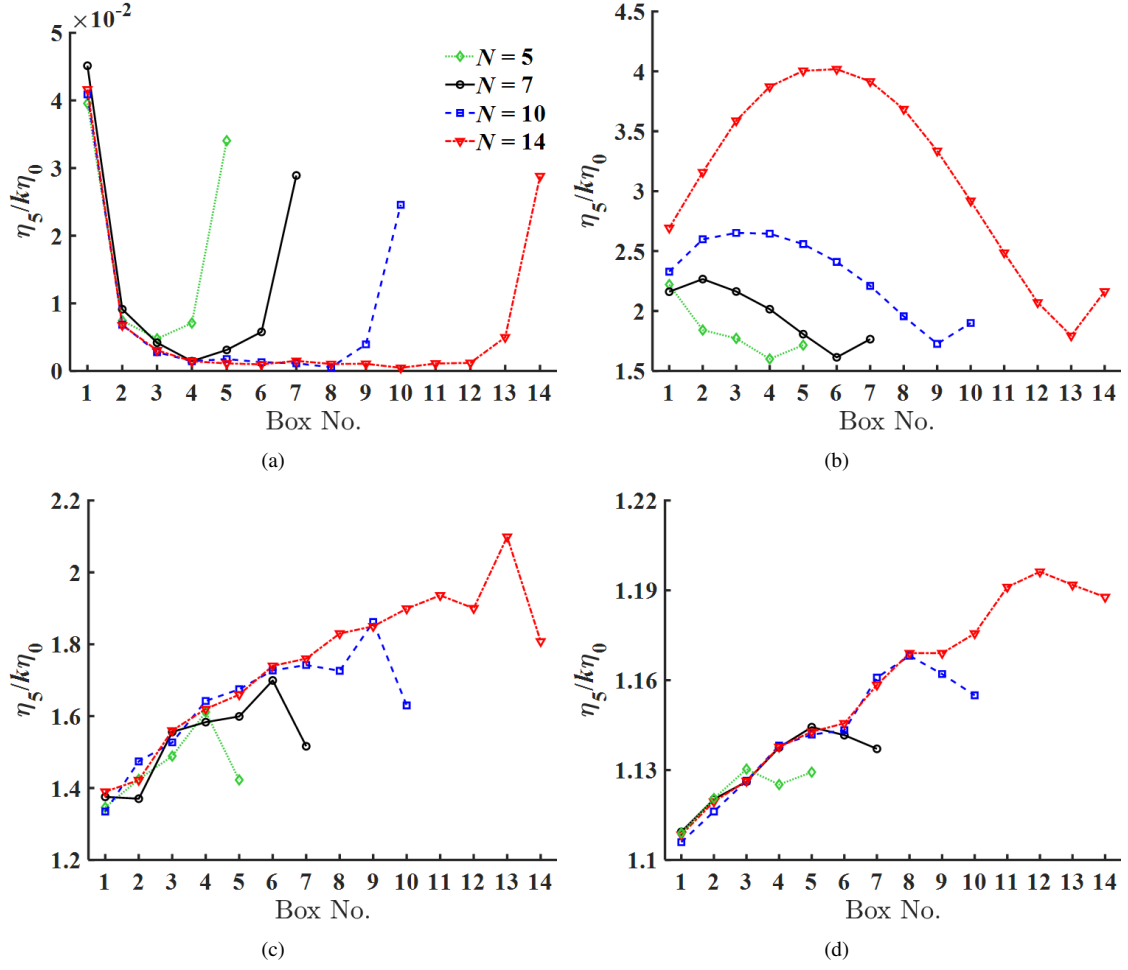
FIG. 14. Pitch motion of four arrays with different number of hinged boxes at four typical wavelengths. (a) λ/L=1.1; (b) λ/L=2.4; (c) λ/L=3.8; (d) λ/L=7.6.
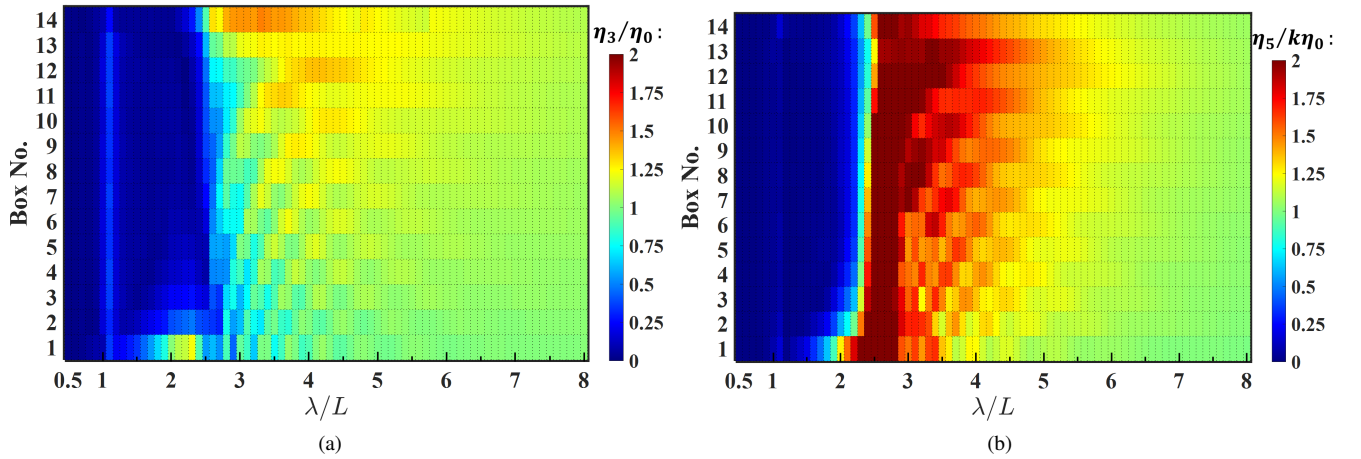

FIG. 15. Heave and pitch motion of hinged 14-boxes arrays. The heave motion is non-dimensionalized by the wave amplitude η_0 and the pitch motion is non-dimensionalized by the wave steepness $k\eta_0$. (a) Heave motion; (b) pitch motion.
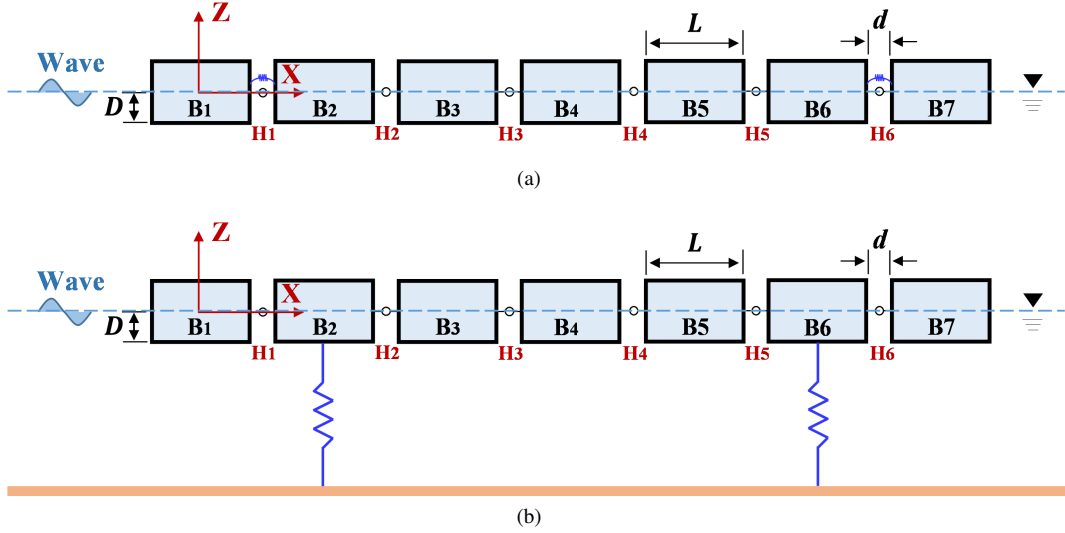
FIG. 16. Sketch of a 7×1 hinged boxes array with two kinds of external stiffness constraints. (a) Rotational spring constraints symmetrically assembled at H1 and H6; (b) vertical mooring constraints symmetrically assembled at B2 and B6.

that longer hinged arrays exhibit larger responses at the trailing end in long waves, as shown in Fig. 13 (c) and (d) and Fig. 14 (c) and (d). However, when the responses of the entire array are very strong, as shown in Fig. 13 (b) and Fig. 14 (b), the motion responses of the arrays consisting of different number of floaters no longer overlap, but still show the exactly identical trend along the longitudinal direction of the arrays. It can be concluded from the numerical case study that the response trend of a shorter array can be used to characterize the response trend of an array with more floaters. However, the number of floaters in such a short array should not be too small, as the response trend at certain locations may not be accurate enough in an array that is too short.

Fig. 15 presents the non-dimensionalized heave and pitch motions of a hinged 14-box array. As can be seen from Fig. 9 (b), (d) and Fig. 15, although the number of floaters in the two arrays differs, they still display a generally similar performance over the entire range of wavelengths. For the heave motion, both arrays exhibit a small response peak around the wavelength of λ/L=1.1. Additionally, a distinct peak can be observed near the wavelength λ/L=2.2 for the first floater in both arrays, and a prominent peak can also be found for the last floater in the wavelength range of λ/L=2.8-4.3. For the pitch motion, strong responses can be found for both arrays in the wavelength range of λ/L=2.3-5. From Fig. 9 (d) and Fig. 15 (b), it is clear that with increasing the floater number (No.1 - No,14), the red and orange regions in the upper-middle position of the motion colormap become broader. It indicates that the floaters at the aft end of the array will have strong pitch motions over a wider wavelength range, highlighting the importance of monitoring the responses of the last couple of floaters in the array. Moreover, an apparently larger red region observed in the 14-box array suggests that a greater number of floaters will lead to stronger pitch motion responses when the array experiences significant motion. This finding is consis-

tent with the above conclusion drawn from Fig. 14 (b). As can also be seen from Fig. 13 (c), (d) and Fig. 14 (c), (d) that the heave and pitch motions of the floaters located at the trailing end of the array become increasingly strong as the number of hinged floaters increases, when the wavelength exceeds the range of the intense motion responses of the entire hinged array.

### C. External stiffness constraints effect

The motion performance of a hinged array can be significantly affected by other external constraints, among which external stiffness constraints are very common. There are two commonly used external stiffness constraints: one is the rotational spring located at the hinge, and the other is the vertical mooring connecting the floater to the seabed, as shown in Fig. 15. The stiffness of the former is added to the motion equations of the two floaters connected by the spring, while the stiffness of the latter is only applied to the equation of the one floater connected to the vertical mooring constraint.

1. Effect of rotational spring stiffness

Fig. 17 and Fig. 18 show the heave and pitch motions of a hinged 7-box array with rotational springs applied symmetrically at different positions. The comparison between the black and blue solid lines indicates that the motion performance of the entire array is highly sensitive to the external spring stiffness, as even a spring stiffness as low as $0.1K_{55}$ leads to significant changes in the array's motion response. Here, K_{55} denotes the hydrostatic restoring stiffness of a modularized box in the pitch direction. It can also be noticed that, except for the case where springs are continuously applied at H3 and
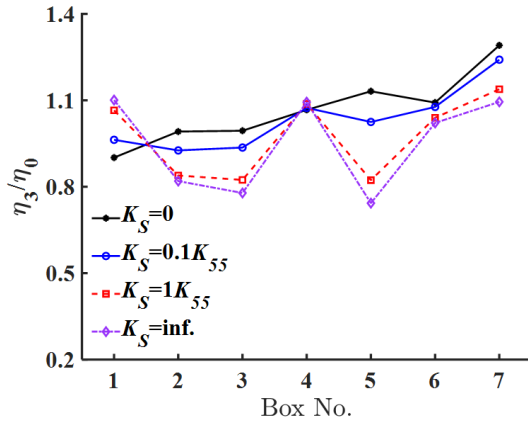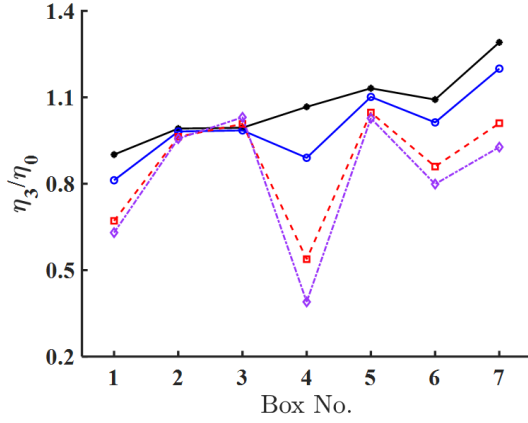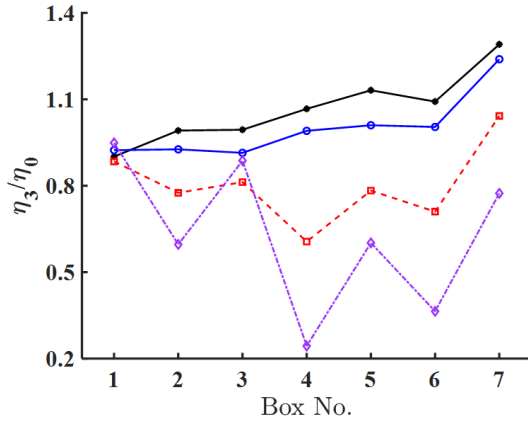
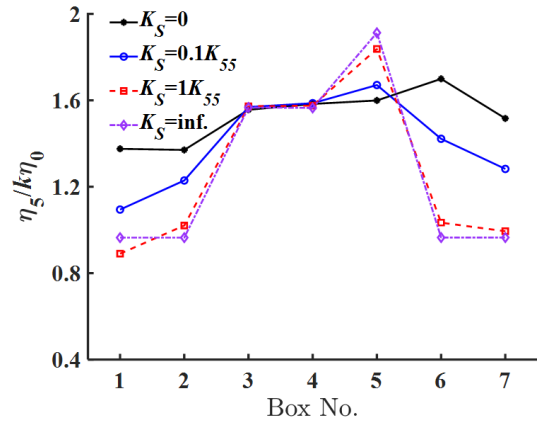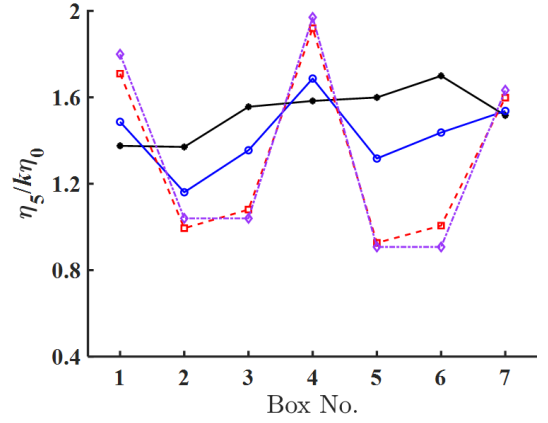FIG. 17. Heave motion of the hinged 7 boxes with different spring connection positions at λ/L=3.8. (a) Springs are symmetrically assembled at H1 and H6; (b) springs are symmetrically assembled at H2 and H5; (c) springs are symmetrically assembled at H3 and H4.

FIG. 18. Pitch motion of the hinged 7 boxes with different spring connection positions at λ/L=3.8. (a) Springs are symmetrically assembled at H1 and H6; (b) springs are symmetrically assembled at H2 and H5; (c) springs are symmetrically assembled at H3 and H4.

H4 resulting in obvious differences in the motion results corresponding to stiffnesses of $1K_{55}$ and infinity, the difference between the red dashed line and the purple dotted line is very small in all other cases. However, despite the existence of the discrepancies in the motion response at the two stiffnesses, the motion trend along the longitudinal direction of the array
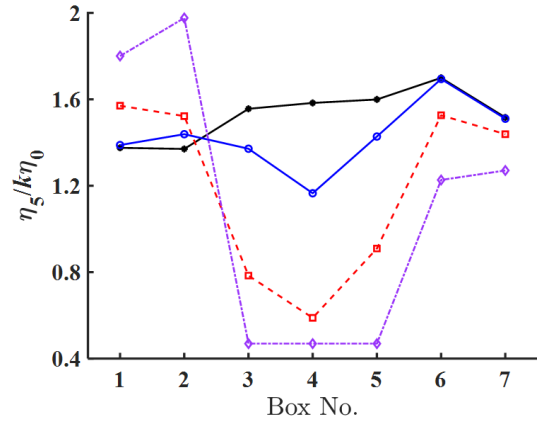
remains consistent. This suggests that it is feasible to achieve motion properties similar to those achieved by applying infinite stiffness without the need for very large spring stiffnesses. From the purple dotted lines in Fig. 18 (b), we can find that the pitch responses of B2 and B3 connected by springs are all smaller than those of B1 and B4, which are adjacent to these
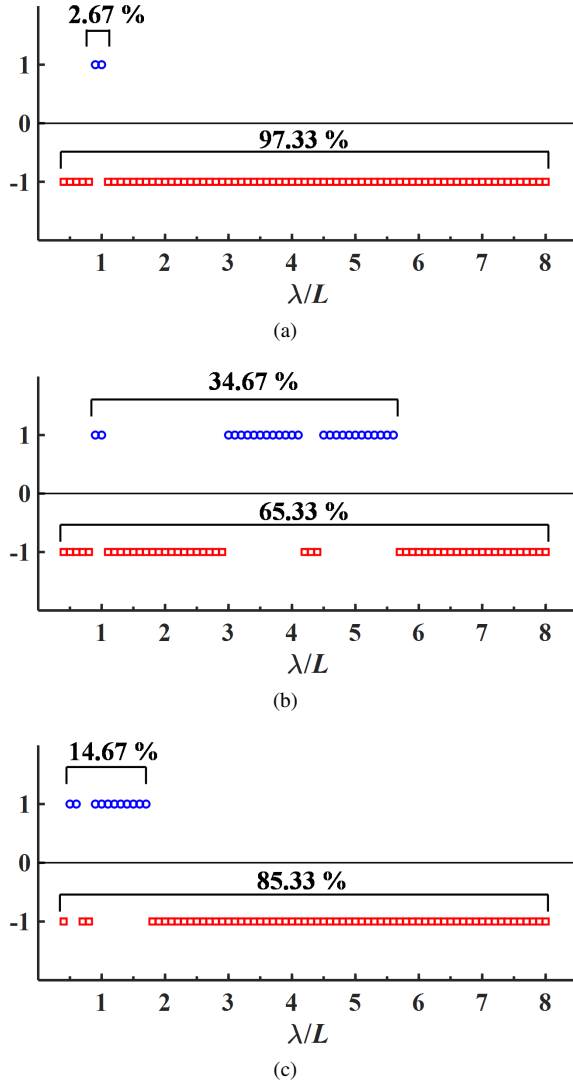
FIG. 19. Statistical results on whether the heave motions of the array with rotational springs satisfy the found trend over the full range of wavelengths. '1' means that the motion response at this wavelength conforms the trend, while '-1' denotes that it deviates from the trend. The springs are assembled at H2 and H5. The statistical conditions are: (a) the response of B1 is lower than that of B2, the response of B7 is less than that of B6; (b) the response of B1 is lower than that of B2; (c) the response of B7 is lower than that of B6.
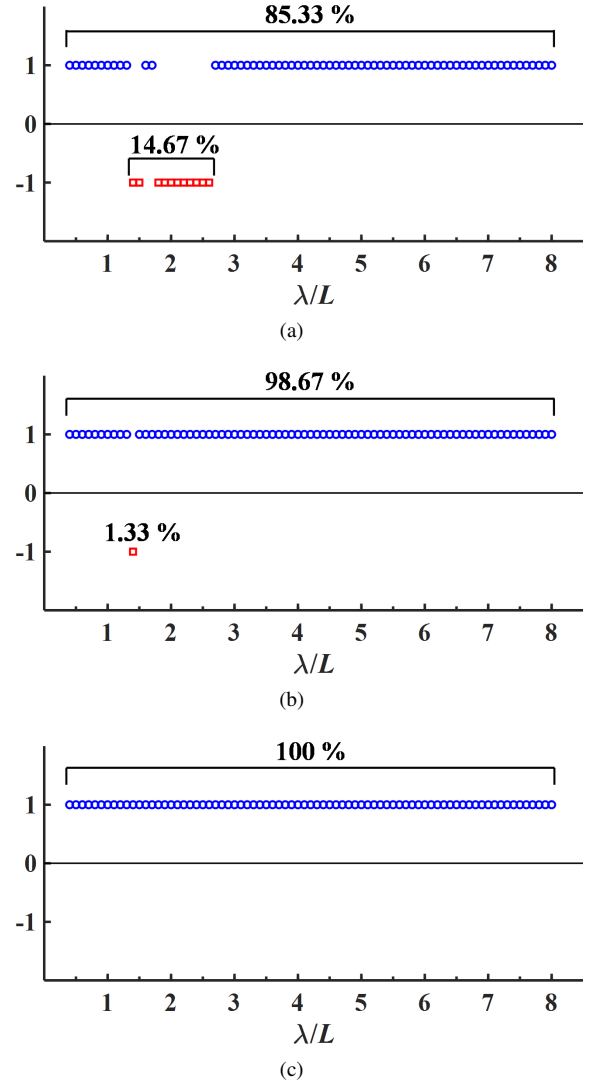
FIG. 20. Statistical results on whether the pitch motions of the array with rotational springs satisfy the found trend over the full range of wavelengths. '1' means that the motion response at this wavelength conforms the trend, while '-1' denotes that it deviates from the trend. The springs are assembled at H2 and H5. The statistical conditions are: (a) the response of B1 is greater than that of B2, the response of B7 is higher than that of B6, and the response of both B3 and B5 are lower than that of B4; (b) the response of B1 is greater than that of B2, the response of B7 is larger than that of B6, and the response of B5 is less than that of B4; (c) the response of B1 is greater than that of B2, the response of B7 is larger than that of B6.

two floaters. Moreover, the pitch responses of B5 and B6 connected by springs are also smaller than those of B4 and B7 adjacent to them. It indicates that the pitch motions of the two floaters connected to the rotational spring are suppressed, while the pitch motions of the floaters adjacent to these two floaters are significantly greater. This phenomenon arises due to the presence of an applied rotational spring, which imparts an additional level of restraint stiffness to the interconnected floating body in the pitch direction. The same properties can also be observed in Fig. 18 (a) and (c). Since the heave motion of the hinged array is coupled with the pitch motion, the heave motion of each module is also affected by the rotational

spring stiffness. As we can see from Fig. 17 (b), when the rotational springs are symmetrically applied at H2 and H5, the heave response of B2 is higher than that of B1, while the heave response of B6 is lower than that of B7. However, in Fig. 17 (a) and (c), the two floaters adjacent to the spring-connected floaters both show larger heave motions, indicating that a clear pattern of the effect of the rotational spring stiffness on the heave motion cannot be summarized from Fig. 17. Fig. 19 and Fig. 20 are used to further investigate the generality of the

impact of rotational spring stiffness on the motion response within the studied wavelength range. If the motion response at a given wavelength satisfies the observed properties, it will be marked as '1' in the figure with a circle dot; otherwise, if it does not follow the summarized patterns, it will be marked with a square dot as '-1'. The rotational springs are assembled at H2 and H5. Compared to the pitch motion in Fig. 20, the statistical results for the heave motion in Fig. 19 are more chaotic, once again indicating there is no clear pattern of the effect of rotational spring stiffness on the heave motion of the hinged array. However, as shown in Fig. 20 (a), the observed characteristics of the impact of rotational spring stiffness on pitch motion occur in 85.33% of the entire wavelength range. Another more easily observed pitch behaviour is that in the floaters adjacent to the spring-connected floaters, the ones towards the ends of the array have a greater response, while the response of the bodies towards the middle position is less than that of the front spring-connected ones but larger than that of the rear spring-connected ones. Combining Fig. 18 and Fig. 20 (c), it can be concluded that when some of the bodies in the hinged array are connected by springs, the ones adjacent to these spring-connected bodies and facing the ends of the array will inevitably have greater pitch responses.

2. Effect of vertical mooring stiffness

Fig. 21 shows the heave and pitch motions of an array of hinged 7-boxes with vertical moorings symmetrically assembled at B2 and B6, as presented in Fig. 16 (b). Even a small external stiffness of $0.1K_{33}$ in the heave direction could cause significant changes in the array's heave and pitch responses, indicating that the responses of hinged arrays are also sensitive to the external stiffness of vertical mooring. When a vertical mooring stiffness of $1K_{33}$ is applied, the heave and pitch responses of the array show the same trend as the array response with an infinite mooring stiffness applied. As can be seen from Fig. 21 (a) that the heave motion of the floater is completely restricted to 0 when an infinite mooring stiffness is applied. This is different from the restriction on pitch motion by an infinite rotational spring stiffness, as illustrated in Fig. 18, where the pitch motion of the hinged array cannot be completely restricted to 0. When an infinite rotational spring stiffness is applied, the two spring-connected bodies will no longer have relative rotation but will rotate together as a single unit. This can explain why the heave motion is completely limited by infinite vertical stiffness, while the pitch motion is not completely restrained by infinite rotational stiffness. Two remarkable peaks can be observed in Fig. 21 (b) at B2 and B6, which indicates that the pitch response of the moored floater with vertical stiffness will be greater than that of the adjacent bodies. Since infinite vertical stiffness inevitably restricts the heave of moored bodies to 0, only the universality of the effect of vertical stiffness on pitch is further investigated here. The statistical results are shown in Fig. 22. It is very interesting to find that the observed pattern holds within the wavelength range of λ/L=2.6-7.2, where the pitch motion of the entire array is relatively significant, as shown in Fig. 9 (d). More-
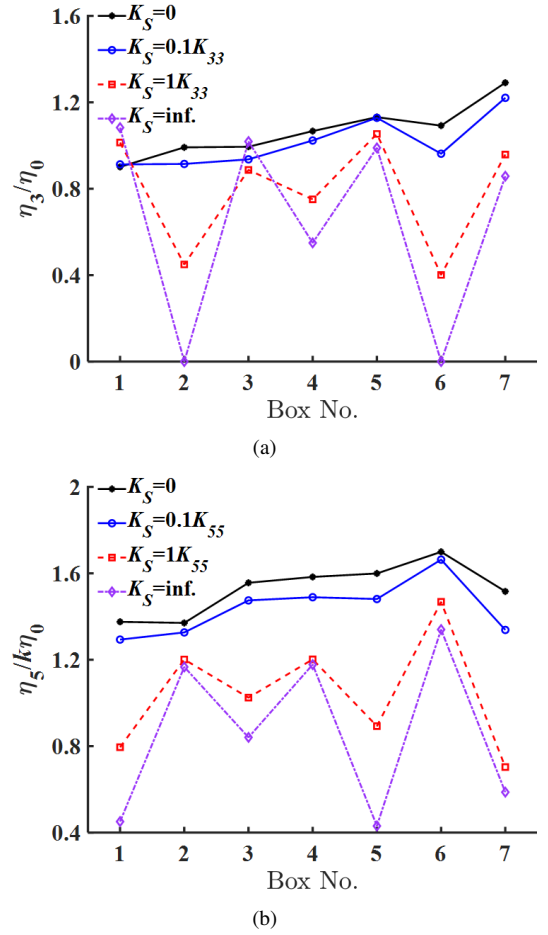

(a)

(b)

FIG. 21. Heave and pitch motion of the hinged 7 boxes with vertical mooring constraints at λ/L=3.8. The vertical mooring constraints are assembled at B2 and B6. (a) Heave motion; (b) pitch motion.

over, the possibility of two other trends is also examined and presented in Fig. 22 (b) and (c), respectively. The results in Fig. 22 (b) are identical to those in Fig. 22 (a), indicating that when the pitch of the moored bodies with vertical stiffness is larger than the response of the adjacent bodies towards to the ends of the array, it will also be greater than that of the adjacent bodies towards the inside of the array. The last trend is that the pitch motion of the floater with vertical mooring stiffness is greater than that of the adjacent floater facing the array's interior. As shown in Fig. 22 (c), this trend occurs at more wavelengths, reaching a proportion of 78.67%.

VI. CONCLUSIONS

In the present study, an in-house 3-D boundary element programme was validated through a model test with a 5-box array, and then applied to model the dynamic motions of large arrays of floating bodies with hinge constraints. Extensive numerical simulations were performed in the frequency-domain to investigate the effects of the hinge constraints, the number of longitudinal modules, and the external stiffness constraints
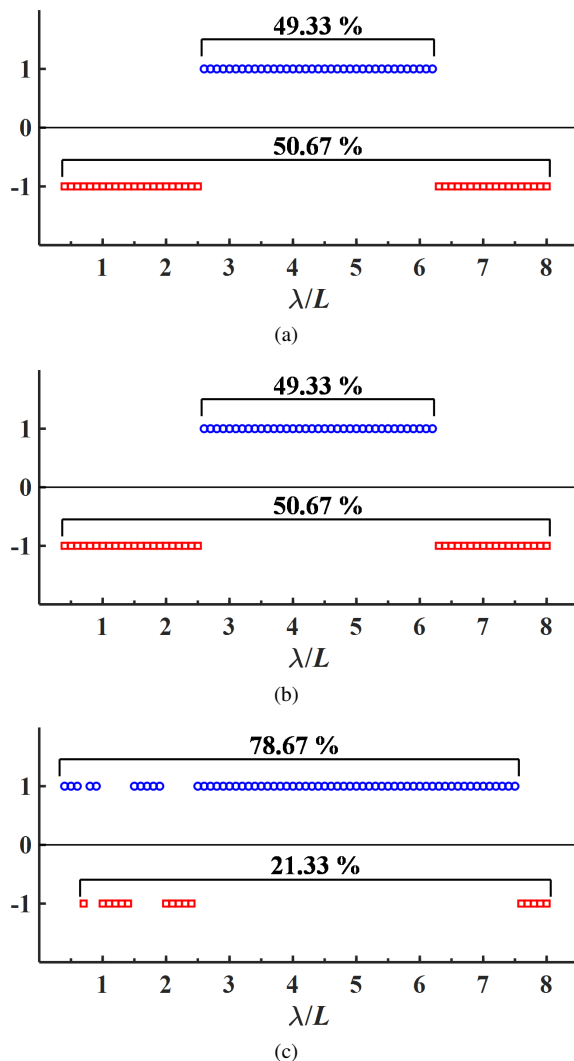
FIG. 22. Statistical results on whether the pitch motions of the array with vertical moorings satisfy the found trend over the full range of wavelengths. '1' means that the motion response at this wavelength conforms the trend, while '-1' denotes that it deviates from the trend. The vertical moorings are assembled at B2 and B5. The statistical conditions are: (a) the response of B2 is larger than that of B1 and B3, the response of B6 is higher than that of B5 and B7; (b) the response of B2 is larger than that of B1, the response of B6 is higher than that of B7; (c) the response of B2 is larger than that of B3, the response of B6 is higher than that of B5.

on the motion responses of hinged arrays. Some conclusions can be drawn as follows.

1) With the application of hinge constraints, the heave motion of the array is significantly suppressed, but strong pitch motion occurs over a wider range of wavelengths. Compared to the responses of an array of floaters with independent oscillations, the motions of the hinged array require longer wavelengths to be significantly excited, and the responses are greater at long wavelengths.

2) The floaters located at the two ends of the hinged array are most likely to be excited with the strongest motion re-

sponses throughout the array, especially the couple of floaters facing the incident waves.

3) The motion response trend along the longitudinal direction exhibited by a shorter hinged array is consistent with that of an array with a greater number of hinged floaters in the longitudinal direction. As the wavelength exceeds the wavelength range of the intense motion responses of the entire array, the motion responses of the floaters at the trailing end of the array become more prominent with an increasing number of hinged floaters.

4) The motion responses of a hinged array are highly sensitive to the external spring stiffness. If some floaters in a hinged array are connected by rotational springs, the floaters adjacent to the ones and facing the ends of the array will inevitably have larger pitch motion responses, but there is no clear regularity of the spring stiffness on the heave response. A high vertical mooring stiffness will cause the heave response of the connected floaters to approach zero, and the most likely performance of its effect on pitch motion is that the response of the connected floaters will be greater than that of the adjacent floaters facing inward toward the array.

The operational performance of hinged arrays is greatly influenced by hydrodynamic interactions and the mechanical coupling effect of connectors. The findings of this study provide valuable insights for optimizing the design and operational strategies, enhancing the efficiency of hinged arrays in engineering applications. In this preliminary study, certain factors such as fluid viscosity, large-area arrangement of modules, and variations in incident wave angles were not specifically examined. Future research will be dedicated to investigating these factors to gain a comprehensive understanding of the motion behaviour of hinged multi-body arrays.

ACKNOWLEDGMENTS

AUTHOR DECLARATIONS

Conflict of Interest

The authors have no conflicts to disclose.

Author Contributions

Deqing Zhang: Conceptualization (equal), Formal analysis (equal), Investigation (equal), Methodology (equal), Software (equal), Validation (equal), Writing - original draft (equal). **Junfeng Du:** Conceptualization (equal), Investigation (equal), Supervision (equal), Writing - review & editing (equal). **Zhiming Yuan:** Conceptualization (equal),

DATA AVAILABILITY STATEMENT

The data that support the findings of this study are available from the corresponding author upon reasonable request.

REFERENCES

[1] H. Behera, C.-O. Ng, and T. Sahoo, "Oblique wave scattering by a floating elastic plate over a porous bed in single and two-layer fluid systems," Ocean Engineering **159**, 280–294 (2018).

[2] S. A. Selvan and H. Behera, "Wave energy dissipation by a floating circular flexible porous membrane in single and two-layer fluids," Ocean Engineering **206**, 107374 (2020).

[3] R. Gayathri, M. B. Khan, H. Behera, and C.-C. Tsai, "Wave attenuation by a submerged circular porous membrane," Journal of Ocean Engineering and Science (2022).

[4] M. M. Hossain, C.-C. Tsai, and H. Behera, "Instability mechanism of shear-layered fluid in the presence of a floating elastic plate," Physics of Fluids **35**, 027102 (2023).

[5] H. Liang, S. Zheng, Y. Shao, K. H. Chua, Y. S. Choo, and D. Greaves, "Water wave scattering by impermeable and perforated plates," Physics of Fluids **33**, 077111 (2021).

[6] Z. Liu and Y. Wang, "Numerical studies of submerged moored box-type floating breakwaters with different shapes of cross-sections using sph," Coastal Engineering **158**, 103687 (2020).

[7] R. Halder, M. Damodaran, and B. Khoo, "Deep learning-driven nonlinear reduced-order models for predicting wave-structure interaction," Ocean Engineering **280**, 114511 (2023).

[8] K. Shi and R. Zhu, "Efficient spectral coupled boundary element method for fully nonlinear wave–structure interaction simulation," Physics of Fluids **35** (2023).

[9] H. Kagemoto and D. K. Yue, "Interactions among multiple three-dimensional bodies in water waves: an exact algebraic method," Journal of Fluid Mechanics **166**, 189–209 (1986).

[10] M. Ohkusu, "Hydrodynamic forces on multiple cylinders in waves," in *Proceedings of International Symposium on the Dynamics of Marine Vehicles and Structures in Waves* (Institute of Mechanical Engineers, 1974).

[11] M. J. Simon, "Multiple scattering in arrays of axisymmetric wave-energy devices. part 1. a matrix method using a plane-wave approximation," Journal of Fluid Mechanics **120**, 1–25 (1982).

[12] J.-S. GOO and K. YOSHIDA, "A numerical method for huge semisubmersible responses in waves," Transactions-Society of Naval Architects and Marine Engineers **98**, 365–387 (1990).

[13] B. Borgarino, A. Babarit, and P. Ferrant, "Impact of wave interactions effects on energy absorption in large arrays of wave energy converters," Ocean Engineering **41**, 79–88 (2012).

[14] D. Zhang, Z.-M. Yuan, J. Du, and H. Li, "Hydrodynamic modelling of large arrays of modularized floating structures with independent oscillations," Applied Ocean Research **129**, 103371 (2022).

[15] Wadam, "Wave analysis by diffraction and morison theory," SESAM user manual (2019).

[16] I. Diamantoulaki and D. C. Angelides, "Analysis of performance of hinged floating breakwaters," Engineering Structures **32**, 2407–2423 (2010).

[17] S. Zheng, Y. Zhang, and W. Sheng, "Maximum theoretical power absorption of connected floating bodies under motion constraints," Applied Ocean Research **58**, 95–103 (2016).

[18] E. Loukogeorgaki, E. N. Lentsiou, M. Aksel, and O. Yagci, "Experimental investigation of the hydroelastic and the structural response of a moored pontoon-type modular floating breakwater with flexible connectors," Coastal Engineering **121**, 240–254 (2017).

[19] H. Zhao, D. Xu, H. Zhang, S. Xia, Q. Shi, R. Ding, and Y. Wu, "An optimization method for stiffness configuration of flexible connectors for multi-modular floating systems," Ocean Engineering **181**, 134–144 (2019).

[20] S. Xia, D. Xu, H. Zhang, Q. Shi, G. Wen, and Y. Wu, "Motion mitigation of hinged floating structures by adaptive control," Ocean Engineering **216**, 107700 (2020).

[21] C. Ma, C.-W. Bi, Z. Xu, and Y.-P. Zhao, "Dynamic behaviors of a hinged multi-body floating aquaculture platform under regular waves," Ocean Engineering **243**, 110278 (2022).

[22] J. N. Newman, "Wave effects on deformable bodies," Applied Ocean Research **16**, 47–59 (1994).

[23] L. Sun, R. E. Taylor, and Y. S. Choo, "Responses of interconnected floating bodies," The IES Journal Part A: Civil & Structural Engineering **4**, 143–156 (2011).

[24] S.-M. Zheng, Y.-H. Zhang, Y.-L. Zhang, and W.-A. Sheng, "Numerical study on the dynamics of a two-raft wave energy conversion device," Journal of Fluids and Structures **58**, 271–290 (2015).

[25] N. Ren, C. Zhang, A. R. Magee, Ø. Hellan, J. Dai, and K. K. Ang, "Hydrodynamic analysis of a modular multi-purpose floating structure system with different outermost connector types," Ocean Engineering **176**, 158–168 (2019).

[26] C. Jiang, O. El Moctar, and T. E. Schellin, "Hydrodynamic sensitivity of moored and articulated multibody offshore structures in waves," Journal of Marine Science and Engineering **9**, 1028 (2021).

[27] Y. Liu, N. Ren, and J. Ou, "Hydrodynamic analysis of a hybrid modular floating structure system under different wave directions," Applied Ocean Research **126**, 103264 (2022).

[28] I. B. S. Bispo, S. C. Mohapatra, and C. G. Soares, "Numerical analysis of a moored very large floating structure composed by a set of hinged plates," Ocean Engineering **253**, 110785 (2022).

[29] D.-Q. Zhang, J.-F. Du, Z.-M. Yuan, M. Zhang, and F.-S. Zhu, "Hydrodynamic modelling of modularized floating photovoltaics arrays," in *Proceedings of the 42nd International Conference on Ocean, Offshore and Arctic Engineering* (Melbourne, Australia, 2023).

[30] M. Flikkema, M. Breuls, R. Jak, R. de Ruijter, I. Drummen, A. Jordaens, F. Adam, K. Czapiewska, F.-Y. Lin, D. Schott, *et al.*, "Floating island development and deployment roadmap," Tech. Rep. (Technical Report, 2021).

[31] Z.-M. Yuan, A. Incecik, S. Dai, D. Alexander, C.-Y. Ji, and X. Zhang, "Hydrodynamic interactions between two ships travelling or stationary in shallow waters," Ocean Engineering **108**, 620–635 (2015).

[32] Z.-M. Yuan, C.-Y. Ji, A. Incecik, W. Zhao, and A. Day, "Theoretical and numerical estimation of ship-to-ship hydrodynamic interaction effects," Ocean Engineering **121**, 239–253 (2016).

[33] L. J. Yiew, L. Bennetts, M. Meylan, G. Thomas, and B. French, "Wave-induced collisions of thin floating disks," Physics of Fluids **29**, 127102 (2017).

[34] ITTC, "Recommended procedures and guidelines 7.5-02-07-03.2: Analysis procedure for regular wave tests," Tech. Rep. (Technical Report, 2002).